analytical chemistry

Article

pubs.acs.org/ac

Development of a Versatile in Vitro Platform for Studying Biological Systems Using Micro-3D Printing and Scanning Electrochemical Microscopy

Jiyeon Kim,[†,¶] Jodi L. Connell,[‡,¶] Marvin Whiteley,*[,‡] and Allen J. Bard*[,†]

[†]Department of Chemistry, The University of Texas at Austin, Austin, Texas 78712, United States

[‡]Department of Molecular Biosciences, Institute of Cellular and Molecular Biology, Center for Infectious Disease, The University of Texas at Austin, Austin, Texas 78712, United States

ABSTRACT: We report a novel strategy for studying a broad range of cellular behaviors in real time by combining two powerful analytical techniques, micro-3D printing and scanning electrochemical microscopy (SECM). This allows one, in microbiological studies, to isolate a known number of cells in a micrometer-sized chamber with a roof and walls that are permeable to small molecules and observe metabolic products. In such studies, the size and spatial organization of a population play a crucial role in cellular group behaviors, such as intercellular interactions and communication. Micro-3D printing, a photolithographic method for constructing cross-linked protein microstructures, permits one to compartmentalize a small population of microbes by forming a porous roof and walls around cells in situ. Since the roof and walls defining the microchamber are porous, any small molecules can freely diffuse from the chamber to be detected and quantified using SECM. The size of the chamber and the roof permeability can be obtained by SECM using a small probe molecule, ferrocenemethanol (FcMeOH). The chamber permeability to FcMeOH can be tuned by varying printing parameters that influence the cross-linking density of the proteinaceous material. These analyses establish a versatile strategy as a sensitive platform to quantitatively monitor small molecules produced by microbes.

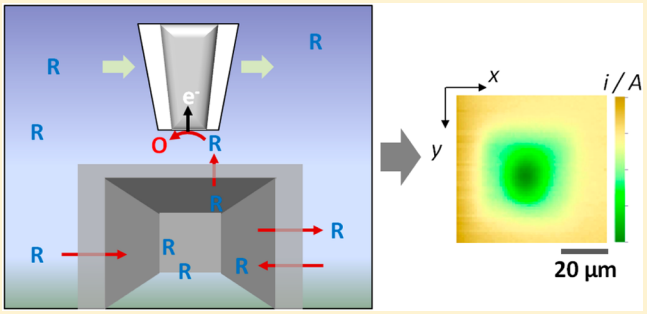

Scanning electrochemical microscopy (SECM) has been widely applied to studies of various biological samples, e.g., DNA,[1] mammalian cells,[2,3] cancer cells,[4] neurons,[5−10] and individual nuclei[11] to understand cellular heterogeneity, activity, communication, neurotransmission, or wall permeability at the single cell level. It, thus, provides a deeper insight into cellular biological processes. SECM is a scanning probe technique, where the ultramicroelectrode (UME) is used as a probe to electrochemically sense redox-active species of interest near a target substrate.[12] In SECM, the probe tip is positioned above the surface of a single cell at a defined distance, or scanned over it, while the electrochemical response is recorded. Hence, one can study the local reactivity or topography of cells beneath the probe with high spatial resolution. Moreover, the probe response can be quantitatively analyzed to extract kinetic and thermodynamic information from the redox reactions of the cells. Especially, the noncontact approach of SECM is suitable for noninvasive observation in single cell studies.[13]

Such biological studies using SECM have been extended to microbiology. Owing to the high spatial resolution as well as the high sensitivity of SECM, spatial profiles of metabolites produced by a bacterial biofilm containing more than 10^8 bacteria could be studied in real time.[14,15] SECM studies of small populations in microbiology has been challenging due to the rapid growth rate of microbes (i.e., 1 to 2 h) compared to other cell cultures[16] without the ability to control the spatial organization and number of cells. Consequently, these technical difficulties associated with manipulating a small population of microbes and their spatial organization have limited our understanding of the mechanisms controlling cellular behavior and their interactions within the microenvironment.

Recently, micro-3D printing, a lithographic method, showed the capability to successfully compartmentalize a small cell population in situ and control their organization by printing protein-based walls around a few cells.[17,18] These fabricated micrometer-sized chambers are robust enough to entrap the microbes without escape but are sufficiently porous to allow small molecules to freely diffuse out of the chamber, which makes this platform useful for SECM studies.

Here, we report a novel strategy for studying a broad range of cellular behaviors in real time by combining two powerful analytical techniques, micro-3D printing and SECM. In this initial work, we employ SECM to quantitatively characterize the 3D printed protein material in order to interface these techniques for cellular applications. 3D printed chambers, similar to "microtraps" used to study bacterial aggregates,[17−19]

Received: September 26, 2014
Accepted: November 17, 2014
Published: November 17, 2014

were characterized by SECM to evaluate their dimensions and the permeability to a small probe molecule, ferrocenemethanol (FcMeOH). The high permeability and the accurate height of the microchamber were successfully measured by SECM and theoretically analyzed using finite element simulation. Additionally, we show that the chamber permeability to FcMeOH can be controlled by varying printing parameters that influence the cross-linking density of the protein material. The quantitative analysis of the chambers fabricated using various printing conditions enabled us to evaluate each chamber and select the most suitable fabrication parameters for reproducible measurements. These analyses establish a versatile strategy as a sensitive platform to quantitatively monitor small molecules produced by small populations of microbes confined in microchambers. This coupled approach extends the utility of both micro-3D printing and SECM as tools for studying biological systems and provides a means to examine how one group of cells interacts with other cells in space at the molecular level in real time. Such an approach utilizing these combined techniques has been used to characterize how small bacterial aggregates communicate within a spatially structured microenvironment.[20]

EXPERIMENTAL SECTION

Chemicals. Ferrocenemethanol (97%, FcMeOH; 335061), Gelatin type A (G2500), and Rose Bengal (330000) were purchased from Sigma-Aldrich (St. Louis, MO). Lab-Tek four-well chambered coverglass (#1 borosilicate; 12-565-401) was obtained from Fisher Scientific. BSA (BAH64-0100) was obtained from Equitech-Bio. All reagents were stored according to the supplier's specifications and used as received. Millipore water (>18 MΩ-cm) was used in all experiments. All electrolyte solutions were filtered using a 0.22 μm pore size Millex filter unit (Merck Millipore Ltd., Germany). All experiments were performed in a 1/15 (v/v) mixture of Luria–Bertani (LB) broth (5 g/L yeast extract, 10 g/L tryptone, and 10 g/L NaCl)[21] and morpholinepropanesulfonic acid (MOPS) minimal medium (50 mM MOPS, 43 mM NaCl, 93 mM NH_4Cl, 2 mM KH_2PO_4, 3.5 mM $FeSO_4$, and 1 mM $MgSO_4$) buffered to pH 7.2[22] with 20 mM sodium succinate. We chose this particular medium for future cellular applications since it is suitable for bacterial growth and cell culture.

Instrumentation. Electrochemical measurements were performed using a CHI model 920C potentiostat (CH Instruments, Austin, TX) with the two-electrode cell placed in the grounded stage. Ag/AgCl in a saturated KCl solution was used as a reference and counter electrode. The Pt UME as an SECM probe was obtained using a dual beam instrument (FEI Strata DB235 dual beam scanning electron microscope/focused ion beam). For SECM approach curve measurements, a video-microscope (CCD camera (Infinity 2-1), Caltex lens (VZ-400)) was used.

Micro-3D Printing. Photo-cross-linked protein microchambers were printed directly on the untreated borosilicate surface within a 0.8 mL well of a Lab-Tek chambered #1 coverglass using a dynamic mask-based multiphoton lithography technique as described in detail previously.[23,24] Here, the output from a mode-locked titanium:sapphire (Ti:S) laser (Tsunami; Spectra Physics) tuned to 740 nm was aligned into a dual-axis scanning galvo mirror system (GVS002; Thorlabs, Inc.) that raster-scanned the beam over the face of the digital micromirror device (DMD; 800 × 600 SVGA; Texas Instruments) displaying binary mask images. The reflected Ti:S beam was expanded, collimated, and directed to overfill the back aperture of an Olympus PlanApo 60×, 1.4 N.A. oil-immersion objective placed on a Zeiss Axiovert inverted microscope. 3D printing was done in a layer-by-layer manner at a rate of 2.5–3.0 s per layer using a motorized focus driver (Prior Scientific H122) programmed to move the fine focus of the microscope in the optical (z) axis in defined steps between each horizontal layer. All microchambers were printed to have an 8 pL inner chamber measuring 20 × 20 × 20 μm ($l \times w \times$ nominal height) with four, 8 μm thick walls, a roof with a nominal thickness of 3 μm, and outer dimensions of 36 × 36 × 23 ($l \times w \times$ nominal height), as shown in Figure 1a, at room

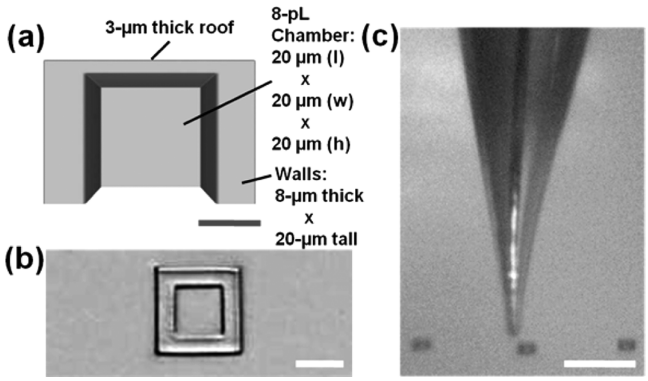

Figure 1. (a) Schematic of a cut-out front view of the 3D printed microchamber designed for SECM studies. The 8 pL inner chamber is 20 × 20 × 20 μm ($l \times w \times$ nominal height), and the outer dimensions are 36 × 36 × 23 μm ($l \times w \times$ nominal height). The 8 pL chamber is a closed system that is anchored directly to a coverglass surface on the bottom and then surrounded by four, 8 μm thick walls and a 3 μm thick roof composed of photo-cross-linked protein. Scale bar, 10 μm. (b) Bright-field image of the microchamber. The 3 μm thick roof is optically transparent and not visible in the image. Scale bar, 20 μm. (c) Video-microscope image of a 5 μm diameter SECM tip positioned adjacent to an 8 pL 3D printed protein microchamber. Scale bar, 100 μm.

temperature using an average laser power of 40 mW measured at the back aperture of the objective. Unless it is noted otherwise, all microchambers in this work were printed from a precursor solution prepared in a 20 mM HEPES (pH 7.4, 0.1 M NaCl) buffer containing 9 mM Rose Bengal, 200 mg/mL gelatin (Type A; porcine), and 75 mg/mL bovine serum albumin (BSA) using an optical (z) axis step size of 0.25 μm between fabrication layers and a single scan per horizontal layer. Following fabrication, the sample well was washed out with multiple volumes (~0.5 mL each) of HEPES buffer heated to 37 °C until the remaining, uncross-linked gel was removed. After the excess precursor had been removed, each sample was washed in the LB/MOPS medium containing 0.1 mM FcMeOH added as a redox mediator.

For the experiments shown in Figure 5a, the permeability of the microchambers to FcMeOH was increased by altering the printing conditions to decrease the cross-linking density by printing from a fabrication precursor solution prepared in the HEPES buffer described above containing 5 mM Rose Bengal, 200 mg/mL gelatin (Type A; porcine), and 50 mg/mL BSA using an optical (z) axis step size of 0.50 μm between fabrication layers. However, in Figure 5c, the permeability of the microchamber to FcMeOH was decreased by tuning the printing conditions to increase the cross-linking density as a

result of using an optical (z) axis step size of 0.50 μm between fabrication layers and scanning through the microchamber roof a total of three times (instead of once).

Preparation of the SECM Tips. The Pt UMEs were prepared according to a procedure reported elsewhere by laser pulling (Sutter Instruments) followed by milling with a focused ion beam (FIB) (FEI Strata DB235 dual beam SEM/FIB). The radius of the Pt UME was checked electrochemically by cyclic voltammetry with 0.1 mM FcMeOH in MOPS buffer, which was consistent with that measured by SEM.

Quantitative SECM Measurements. All electrochemical measurements were performed using a CHI model 920C potentiostat (CH Instruments, Austin, TX) with the two-electrode cell placed in the grounded stage. Ag/AgCl in a saturated KCl solution was used as a reference and counter electrode. A 5 μm diameter Pt UME was used as the SECM tip, and all electrochemical data was collected at room temperature in the LB/MOPS medium with 0.1 mM FcMeOH added as a redox mediator for accurate tip positioning. The tip was biased at 0.4 V vs Ag/AgCl to oxidize FcMeOH. The tip approach rate was 100 nm/s for all approach curves. All SECM images were obtained by scanning the tip in the x- and y-axes at a rate of 10 μm/s at a fixed height of 2 μm above the chamber roof.

SECM Approach Curve Measurements and SECM Imaging. To obtain the SECM approach curves or SECM imaging using the prepared Pt UME, the tilt of glass substrate was adjusted using two steps. First, using the leveler, the substrate tilt was adjusted coarsely. Then, the coarsely adjusted tilt was finely controlled using the video-microscope. Since the orientation of the FIB milling was adjusted perpendicularly to the body of the Pt UME, we aligned the substrate perpendicular to the body of the Pt UME in the x- and y-axes using the video-microscope with less than a 0.1 degree offset. This procedure aligns the surface of FIB milled Pt UME parallel to the substrate, thus enabling a closer approach. Furthermore, to avoid electrostatic damage on the electrode surface and thereby maintain the inlaid shape of the Pt UME, we followed the method of the electrostatic damage (ESD) protection reported by Nioradze et al.[25] With all the ESD damage protection, the SECM measurement was carried out in a humidity controlled room with higher than 30% relative humidity at 22−23 °C.

RESULTS AND DISCUSSION

Microchamber Design and Visual Characterization Using Optical and Video Microscopy. The 3D printed microchambers were observed under an optical microscope to ensure the final dimensions and structure after fabrication. As shown in Figure 1a,b, the final dimensions of the chamber under the optical microscope was consistent with the original design of inner dimensions (ID) of 20 × 20 × 20 μm ($l \times w \times$ nominal height) and outer dimensions (OD) of 36 × 36 × 23 μm ($l \times w \times$ nominal height) to afford an inner chamber volume of 8 pL. The 8 μm-thick walls and 3 μm-thick roof surrounding the microchamber provide sufficient physical robustness to wash out the excess precursor reagent postfabrication, such that the microchamber remains intact in its original shape without damage. This physical strength is essential for the accurate and reproducible measurements in SECM by forming a stable gap between the SECM tip and a target or substrate. To check the adaptability of the chamber in the SECM setup, we further introduced a video-microscope to visually observe the positioning of the SECM tip near the chamber. The SECM tip was successfully positioned adjacent to the microchamber by the piezo motor under the video-microscope as displayed in Figure 1c. This visual operation of the coarse tip positioning nearby the chamber is helpful to avoid an unwanted tip crash into the target surface during the SECM measurements. In addition, it shortens the SECM experimental time and thus allows for the SECM applicability to study microbiology, where the time span is critical for assessing microbial growth.

In SECM, the height of the microchamber should be accurately measured for the precise tip positioning above it, because the current response is a function of the distance between the tip and the chamber. In this respect, the exact variation from the nominal fabrication height of 23 μm could be measured by SECM as described in the following section.

Characterization of the Microchamber by SECM. *Height of the Microchamber Measured by SECM.* The 3D printed microchamber is porous as a result of its photo-cross-linked protein structure; thus, small molecules can permeate through the pores freely. As the current in the SECM measurements is highly dependent on the distance between the SECM tip and the chamber, it is important to know the accurate height of the chamber. For this purpose, first, the piezo motor was used to position the Pt UME near the chamber under the video-microscope. A FIB-milled Pt UME with a radius (a) of 2.5 μm as surrounded by a thin glass sheath with outer radius (r_g) of 4.2−5.0 μm was used. The general procedure for measuring chamber height is briefly explained below.

First, a SECM approach curve was measured over the insulating glass substrate adjacent to the chamber with the Pt UME biased at 0.4 V vs Ag/AgCl in the presence of FcMeOH. The resultant approach curve follows normal negative feedback due to the hindered diffusion of FcMeOH by the insulating substrate as shown in Figure 2a (black curve). Note that the

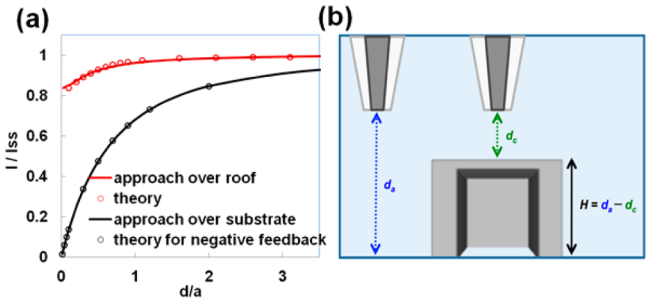

Figure 2. (a) SECM approach curves over the insulating substrate (black curve) adjacent to the chamber and over the roof of the chamber obtained with 0.1 mM FcMeOH as a redox mediator in MOPS buffer. Each curve was fitted with the theoretical curves (open circles). The Pt UME was biased at 0.4 V vs Ag/AgCl. The scan rate was 10 μm/s. (b) Schematic of the chamber height measurement. The difference between the initial tip position from the insulating substrate (d_a) and the tip displacement until the inflection point at the contact moment (d_c) corresponds to the chamber height (H).

FIB-milled Pt UME can approach ~75 nm from the glass substrate without contact (Figure 2a, black curve) showing the remarkable approach capability. On the basis of the feedback current of the Pt UME fitted with a theoretical approach curve, the accurate tip position from the substrate could be calculated. Then, the Pt UME was withdrawn up to 45 μm from the substrate, which is high enough not to crash over the chamber with the approximate OD of 36 × 36 × 23 μm ($l \times w \times$

dx.doi.org/10.1021/ac5036204 | Anal. Chem. 2014, 86, 12327−12333

nominal height). Afterward, the Pt UME was laterally moved toward the chamber by the piezo under a video-microscope. The coarse SECM imaging over the chamber was performed repeatedly from this height by lowering the Pt UME in 1−2 μm steps until the chamber was sensed. This procedure is necessary to align the Pt UME above the center of the chamber roof. Once the Pt UME was positioned over the center of the roof, the Pt UME was withdrawn to the original height (45 μm from the insulating substrate or ∼20 μm above the chamber). Subsequently, another SECM approach curve was measured over the roof of the chamber until the Pt UME contacted the surface of microchamber roof. The contact between the roof surface and the glass sheath surrounding the Pt UME is seen as the inflection point of the experimental approach curve (Figure 2a, red curve). Such an inflection point appears due to the slight contact between the tip and the chamber roof, which causes a deviation from the simulated point near the zero normalized distance (Figure 2a, red open circle). After contacting the roof surface, the Pt UME was immediately withdrawn to the initial height with recovery of the original steady state current, $i_{T,\infty}$. Overall, the difference between the initial tip position (d_a) over the insulating substrate and the tip displacement (d_c) until the inflection point at the contact moment corresponds to the chamber height as a schematic shown in Figure 2b. Accordingly, the measured height of the series of chambers varied, 23.5 ± 1.5 μm, which is consistent with the nominal height as estimated from the 3D printing process.

The analysis of the characteristic approach curve over the chamber is further explained below. When the Pt UME was positioned far from the chamber, the stable steady state current based on the diffusion-limited oxidation of FcMeOH was obtained (eq 1).

$$i_{T,\infty} = 4xnFDc^*a \tag{1}$$

where x is a function of RG (= r_g/a), n is the number of transferred electrons (= 1) in the tip reaction, and D (= 7.4 × 10^{-6} cm^2/s) and c^* (= 0.1 mM) are the diffusion coefficient and the concentration of FcMeOH in the MOPS buffer solution, respectively. The Pt UME radius was determined from $i_{T,\infty}$ using the r_g value in the FIB image of each milled UME. When the Pt UME starts to approach and positions close to the chamber, FcMeOH in the adjacent aqueous solution is steadily depleted, as the Pt UME biased at 0.4 V keeps oxidizing FcMeOH. Consequently, a concentration gradient of FcMeOH is induced by the Pt UME, thus driving the transport of FcMeOH from the inside chamber to the Pt UME surface across the roof. Here, we assume that FcMeOH diffuses freely through the porous matrix of the roof without interacting with the cross-linked material based on two reasons: (1) A Stokes radius of 0.33 nm for FcMeOH is small and the high porosity matrix of cross-linked protein materials has been shown to permit rapid transport of small molecules.[17,26] (2) Any charged parts in the porous structure can be screened by the MOPS buffer with a high ionic strength of ∼0.1 M, thereby exerting a negligible effect on neutral FcMeOH and charged probe molecules. As FcMeOH diffuses freely through pores on the chamber roof and wall, the current decrease with distance in the approach curve could be attributed to the impermeable framework of the chamber. In consequence, the amperometric tip current, i_T, started to decrease significantly at a distance of ∼3 μm (1.2 d/a, normalized distance against Pt UME radius) over the roof (Figure 2a, red curve), which enables us to sense the chamber when the Pt UME approaches or scans over the chamber roof. As the obtained current is the function of the permeability of the roof to FcMeOH as well as the distance between the Pt UME and the roof, the shape of the approach curve is determined by the characteristic permeability of the chamber. We will discuss more details about the permeability and the SECM imaging of the chamber in the next section.

Note that the Pt UME contacted with the roof at a short distance of ∼125 nm, as confirmed by theoretical simulation (COMSOL Multiphysics 4.2a, red open circles on the red curve in Figure 2a). The close contact distance minimizes the uncertainty of the zero distance in the analysis of approach curve, thereby allowing for the accurate measurement of chamber height. Such a close contact could be attributed to the physically robust and smooth surface of the chamber as well as nanolevel smoothness on the Pt surface of the Pt UME and perpendicular alignment of the Pt UME to the surface of the chamber roof.

Determination of the Permeability of the Microchamber to the Probe Molecule, FcMeOH. The permeability of the roof to the probe molecule (FcMeOH) affects the current response of the Pt UME, which is needed to know the distance between the Pt UME and the chamber.[11,12] The permeability of the gelatin chamber was determined by fitting experimental approach curves over the chamber roof to theoretical curves. The theoretical curves were obtained by solving a two-phase SECM diffusion problem using a COMSOL Multiphysics finite element package (version 4.2a, COMSOL, Burlington, MA). In this finite element simulation, normalized parameters were employed, where the normalized chamber permeability, K, was defined as eq 2:

$$K = \frac{k_{\text{chamber}}a}{D_{\text{M}}} \tag{2}$$

where a is the radius of the Pt UME and D_{M} is the diffusion coefficient of FcMeOH in MOPS buffer. Thus, the chamber was treated as a uniform surface with a distinct permeability, k_{chamber}, as given by eq 3,

$$\text{FcMeOH (outer)} \underset{k_{\text{chamber}}}{\overset{k_{\text{chamber}}}{\rightleftharpoons}} \text{FcMeOH (inner)} \tag{3}$$

where the equal permeability for the inflow and outflow corresponds to the same equilibrium concentration of FcMeOH in the bulk outer MOPS buffer solution and the chamber inside. The diffusion of FcMeOH in the outer MOPS buffer solution and the MOPS buffer solution in the chamber was defined by eqs 4 and 5,

$$\frac{\partial c_{\text{oc}}(x,y,z)}{\partial t} = D_{\text{M}}\left[\frac{\partial^2 c_{\text{oc}}(x,y,z)}{\partial x^2} + \frac{\partial^2 c_{\text{oc}}(x,y,z)}{\partial y^2} + \frac{\partial^2 c_{\text{oc}}(x,y,z)}{\partial z^2}\right] \tag{4}$$

$$\frac{\partial c_{\text{ic}}(x,y,z)}{\partial t} = D_{\text{M}}\left[\frac{\partial^2 c_{\text{ic}}(x,y,z)}{\partial x^2} + \frac{\partial^2 c_{\text{ic}}(x,y,z)}{\partial y^2} + \frac{\partial^2 c_{\text{ic}}(x,y,z)}{\partial z^2}\right] \tag{5}$$

where $c_{\text{oc}}(x,y,z)$ and $c_{\text{ic}}(x,y,z)$ are the concentrations of FcMeOH in the MOPS buffer solutions outside and inside the

dx.doi.org/10.1021/ac5036204 | Anal. Chem. 2014, 86, 12327−12333

chamber, respectively, and D_M is the diffusion coefficient of FcMeOH in the MOPS buffer solutions at both sides of the chamber. Initially, the MOPS buffer solution on both sides of the chamber contained FcMeOH at a bulk concentration of c*. The oxidation of FcMeOH at the Pt UME over the roof was limited by the diffusion of FcMeOH, which resulted in the depletion in the adjacent aqueous solution. The resulting concentration gradient induced the transport of FcMeOH through the pores from the inside of the chamber (Figure 3a). The boundary condition at the chamber was given by eq 6,

$$D_M\left[\frac{\partial c_{oc}(x, y, z)}{\partial z}\right]_{z=0} = D_M\left[\frac{\partial c_{ic}(x, y, z)}{\partial z}\right]_{z=0} = k_{chamber}[c_{oc}(x, y, 0) - c_{ic}(x, y, 0)] \quad (6)$$

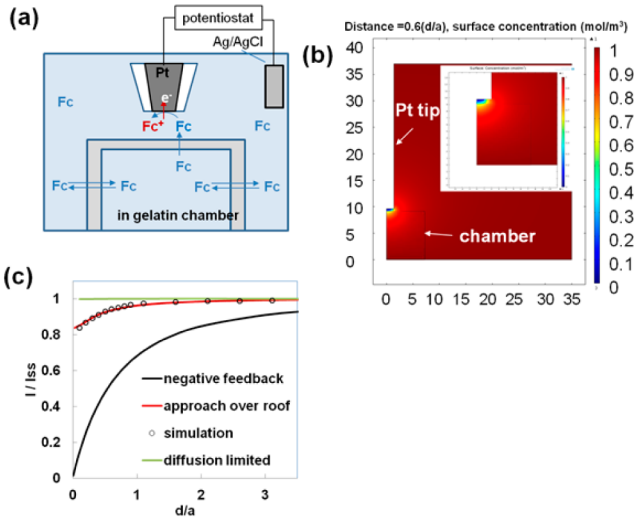

Figure 3. (a) Illustration of the FcMeOH permeability measurement for the chamber using a Pt UME. (b) 2D axial symmetric cross section of the concentration profile of FcMeOH around the Pt tip−chamber roof as simulated by the finite element analysis when the tip is held at the normalized height, d/a = 0.8. The inset magnifies the discontinuous concentration gradient under the tip across the chamber. The permeability of k = 0.12 cm/s is defined at the chamber wall and roof. (c) The experimental (red curve) and the simulated (open black circles) approach curves over the chamber roof and the insulating substrate (black curve). The green curve represents the diffusion-limited case (i.e., no kinetic effect). The respective simulation curve employed a = 2.5 μm with RG 1.4 (open black circles).

As FcMeOH diffuses freely through pores on the chamber roof and wall, a kinetic effect observed in an approach curve is attributed to a diffusion barrier posed by the photo-cross-linked matrix of the chamber. Figure 3b presents this kinetic effect as the local discontinuity in the concentration profile of FcMeOH across the chamber roof under the tip. The experimental approach curves fitted well with the simulated approach curves to obtain the chamber permeability, $k_{chamber}$, of 0.12 (±0.01) cm/s (Figure 3c, red curve fitted with open circles). In fact, the mass transfer coefficient at the nanogap of 125 nm between the Pt UME and the chamber roof, D/d of 0.61 cm/s, is higher than the $k_{chamber}$ by a factor of ∼5. In this condition, we ensure that our measurement is in the kinetically limited regime, thus confirming the reliability of the high permeability values measured using SECM. In addition, the numerical analysis also shows that the contact of the Pt UME with the chamber roof was made within the nanometer gap of ∼125 nm, which was critical for an accurate measurement of the chamber permeability to FcMeOH as well as the chamber height with minimum uncertainty in the zero distance of the approach curves.

SECM Imaging of the Microchamber Based on an Induced Transport of FcMeOH. In addition to the structural characterization of the microchamber, SECM was used to generate a transport map over the chamber to the probe molecules. For these experiments, we collected a SECM image of the microchamber at a constant height of 2 μm above the roof in the presence of FcMeOH. The simple schematic for the SECM imaging is illustrated in Figure 4a. The inside of the

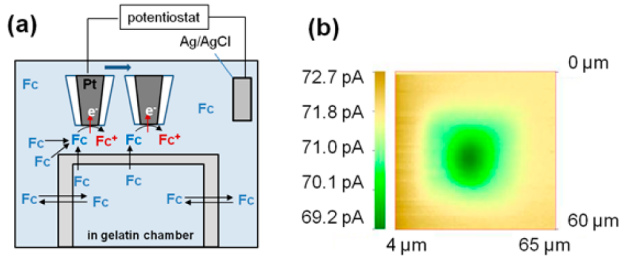

Figure 4. (a) SECM cell with the 3D printed protein microchamber filled with 0.1 mM FcMeOH and MOPS buffer solution. The Pt UME positioned at a constant height of 2 μm above the chamber roof is biased at 0.4 V vs Ag/AgCl to oxidize FcMeOH. (b) SECM image over the chamber in the FcMeOH solution produced by scanning the tip in the $x-y$ direction. The brown color on the current scale represents the highest oxidative current while the green color is the minimum. Tip potential, 0.4 V vs Ag/AgCl. Tip scan rate, 10 μm/s. Pt UME with a = 2.5 μm with RG 1.4 was used for the oxidation of FcMeOH during the SECM image.

chamber is filled with 0.1 mM FcMeOH and MOPS buffer as well as outside, and FcMeOH freely diffuses through the chamber wall and roof. Here, the Pt UME with radius a = 2.5 μm with RG 1.4 is biased at 0.4 V vs Ag/AgCl and scanned over the chamber at a scan rate of 10 μm/s (1 μm/0.1 s). When the Pt UME is far away from the chamber horizontally, the diffusion of FcMeOH to Pt UME is as efficient as in bulk solution since the tip is also far from the insulating substrate as well as the chamber roof; thus, the same current as the limiting current in the bulk solution is obtained. As the Pt UME gets closer to the chamber and is over the edge of the wall, it senses the chamber existence resulting from the delay of FcMeOH diffusion due to its permeability barrier caused by the protein matrix. Still, a significant amount of FcMeOH diffuses efficiently from the other side facing the bulk solution; thus, the tip current slightly decreases over the edge of the chamber. The maximum kinetic effect caused by the framework of the microchamber is observed when the Pt UME is positioned above the center of the roof. At this time, most of the FcMeOH is delivered to the Pt UME surface as a result of the Pt UME-induced transport through the chamber roof. Overall, the tip current reaches a minimum above the center of the roof. The magnitude of the current decrease from the original limiting current is determined by the chamber permeability as well as the gap between the tip and the roof. Thereby, it follows the current behavior shown in the approach curve over the chamber roof (Figure 3c, red curve). A typical SECM image of the chamber is shown in Figure 4b. It should be noted that the

dx.doi.org/10.1021/ac5036204 | Anal. Chem. 2014, 86, 12327−12333

limiting current (I_{ss}) decreased 5% at 2 μm above the center of the chamber with a measured permeability, $k_{chamber}$= 0.12 cm/s, which is consistent with 0.95 of the normalized current (I/I_{ss}) at 0.8 of the normalized distance (d/a) in the SECM approach curve over the chamber roof (Figure 3c, red curve).

Tuning the Chamber Permeability to FcMeOH by Modulating the Cross-Link Density of the 3D Printed Protein Matrix and Its Characterization by SECM. A highly permeable chamber is desired not to interrupt the diffusion of the probe molecules during real-time monitoring when these chambers serve as an in vitro platform for biological studies. However, if the photo-cross-linked protein structure is too porous, it can cause great difficulty with the reliable characterization of the structural properties by SECM since the probe molecules would transport through the material as efficiently as the diffusion-limited case. As a result, we would not obtain a noticeable change in the tip current during the approach curve measurement over the chamber (Figure 5d, green curve).

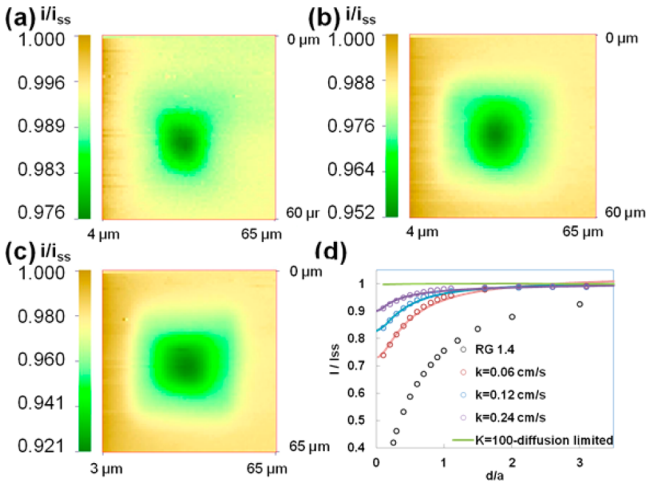

Figure 5. Representative SECM images of microchambers with FcMeOH permeabilities of (a) 0.24, (b) 0.12, and (c) 0.06 cm/s. All the SECM images were measured at 2 μm above the chamber roof with a 2.5 μm radius Pt UME with RG 1.4. The current values are normalized by the limiting current in the bulk solution, I_{ss}. (d) SECM approach curves obtained over the chamber roof for each condition. The permeability to FcMeOH is estimated by fitting the experimental data with finite element simulation.

Thereby, precise tip positioning over the chamber would not be possible since it would be difficult to distinguish the difference between the microchamber and the bulk solution based on the current response in SECM images. Without accurate information about the chamber height and its permeability, a quantitative analysis cannot be achieved. Indeed, the initial photo-cross-linked protein matrix selected for these studies was too porous to be sensed easily in the SECM measurements unless the working distance of the Pt UME over the chamber is within ~1 μm. Without accurate height information, such a close working distance for the SECM measurements easily crashed the Pt tip into the roof. Since the UME, made of glass and metal, is more robust than the chamber made with gelatin, the UME is not physically damaged at all, but only the surface of UME could be fouled by a fragment of gelatin upon the crash of UME with the chamber roof. In contrast, the chamber roof has been dented by the tip crash. To overcome this technical challenge, we took advantage of the versatility offered by the 3D printing technique. Micro-3D printing has the flexibility to tune the porosity of the photofabricated material by modifying the concentration of gelatin, BSA, and the photosensitizer (Rose Bengal) in the precursor solution or varying parameters, such as the average laser power, scan velocity, z-axis step size between fabrication layers, or the total number of scans during printing. Thus, one can easily modulate the cross-linking density within the protein matrix.

Here, we modulated the fabrication parameters to increase the cross-linking density within the protein matrix, thus decreasing the permeability. Relative to the initial conditions used to collect the data shown in Figure 5a (k = 0.24 cm/s; Figure 5d, violet curve), we used a precursor with higher concentrations of photosensitizer (Rose Bengal; 9 mM) and BSA (75 mg/mL) and a smaller z-axis step size between fabrication layers (0.25 μm) to decrease the chamber permeability 2-fold to k = 0.12 cm/s (Figure 5b,d, blue curve) or used a larger z-axis step size between fabrication layers (0.50 μm) but scanned through the roof three times (instead of once) to decrease the chamber permeability 4-fold to k = 0.06 cm/s (Figure 5c,d, red curve). Representative SECM images obtained at 2 μm (d/a = 0.8) above the roof displaying the normalized current response (I/I_{ss}) from each condition are shown in Figure 5a–c. We observed a minimum I/I_{ss} of 0.98, 0.95, and 0.92 above the center of the roof of the chamber in (a), (b), and (c), respectively. Notably, all of the normalized current measurements at the center of each chamber roof are consistent with the values in the corresponding approach curves at d/a = 0.8 (solid lines in Figure 5d), confirming the reliability of the theoretical prediction (Figure 5d, open circles) and the reproducibility of the measurements. This result also demonstrates that the 3D printed structure is physically robust enough to maintain its shape during the measurement, which allows for a quantitative analysis. Clearly, these results establish that the permeability of the microchamber to FcMeOH can be modulated 4-fold simply by adjusting the concentration of the photosensitizer and BSA in the fabrication precursor solution, the z-axis step size between fabrication layers, and the number of scans used to print the roof, as described in the Experimental Section.

As mentioned earlier, chamber (a) was too porous to be sensed easily by SECM at distances greater than 2.5 μm over the roof. Thus, the working distance of Pt UME should range at least 0.5–1.0 d/a from the roof surface. This could make the measurements unnecessarily difficult with a high risk of tip crash. We could measure the permeability from chamber (c) in the wider range of 0.06–0.15 cm/s than other fabrication conditions. Chamber (b) showed highly reproducible permeability (0.12(±0.01) cm/s) during more than 70 measurements including the data shown in Figures 2–5 (k = 0.12 cm/s; Figure 5b,d, blue curve). Due to the 2-fold lower permeability to FcMeOH than chamber (a), the current began decreasing noticeably in the range of 1.0–1.5 d/a over the roof (Figure 5d, blue curve); thus, the chamber could be sensed by the SECM image at a distance of 3–3.5 μm. Consequently, the SECM measurements are fairly convenient without the risk of tip crash. Still, the FcMeOH permeability of 0.12 cm/s from chamber (b) is high enough not to interrupt the diffusion of probe molecules. Considering all these aspects, chamber (b) could be the most suitable for our requirements for SECM study. Recently, we presented the successful cellular application of this in vitro microchamber system to studying bacterial group behaviors.[20]

dx.doi.org/10.1021/ac5036204 | *Anal. Chem.* 2014, 86, 12327–12333

CONCLUSIONS

Herein, we develop a novel strategy for studying a broad range of cellular behaviors in real time by combining two powerful analytical techniques, micro-3D printing and SECM. In this work, 8 pL microchambers were constructed using a protein-based 3D printing technique. The printed protein matrix chamber is highly permeable and does not impede the diffusion of small probe molecules while it has physical robustness and high stability. Owing to the flexibility of this micro-3D printing technique, we could tune the permeability of the chamber roof to FcMeOH 4-fold by modifying the cross-link density within the protein matrix. We employed SECM to quantitatively characterize the microchambers. The height and the permeability of the chamber were successfully measured by SECM and theoretically analyzed using finite element simulation. Such a quantitative analysis was critical to evaluate the chambers fabricated under various conditions and select the conditions most suitable for each research purpose. These analyses establish a versatile strategy as a sensitive platform to quantitatively monitor small molecules produced by microbes confined in a microchamber. This coupled approach extends the utility of both micro-3D printing and SECM as dynamic tools for biological studies and provides a means to examine how groups of cells interact in space at the molecular level in real time. Recently, our parallel work utilizing these techniques in combination shows a successful cellular application to addressing how small bacterial aggregates communicate within a microenvironment.[20]

AUTHOR INFORMATION

Corresponding Authors

*Phone: 512-471-3761. Fax: 512-471-0088. E-mail: ajbard@mail.utexas.edu.

*Phone: 512-471-5493. E-mail: mwhiteley@austin.utexas.edu.

Author Contributions

¶J.K. and J.L.C. contributed equally to this work.

Notes

The authors declare no competing financial interest.

ACKNOWLEDGMENTS

We acknowledge support of this research from the AFOSR MURI (FA9550-14-1-0003) and the Robert A. Welch Foundation (F-0021) (A.J.B.). Also, this work is supported by Grant W911NF-13-1-0199 from the US Army Research Office (M.W.). M.W. is a Burroughs Wellcome Investigator in the Pathogenesis of Infectious Disease. J.L.C. is a Cystic Fibrosis Foundation Ann Weinberg Memorial Postdoctoral Research Fellow. The authors thank Prof. Jason B. Shear for the technical support and allowing us to use the 3D printing equipment in his laboratory.

REFERENCES

(1) Fan, F.-R.F.; Bard, A. J. *Proc. Natl. Acad. Soc. U.S.A.* **1999**, *96*, 14222−14227.

(2) Mirkin, M. V.; Liu, B.; Rotenber, S. A. *Methods Enzymol.* **2002**, *352*, 112−122.

(3) Rotenberg, S. A.; Mirkin, M. V. *J. Mammary Gland Biol. Neoplasia* **2004**, *9*, 375−382.

(4) Shiku, H.; Torisawa, Y. S.; Takagi, A.; Aoyagi, S.; Abe, H.; Hoshi, H.; Yasukawa, T.; Matsue, T. *Sens. Actuators, B* **2005**, *108*, 597−602.

(5) Clark, R. A.; Zerby, S. E.; Ewing, A. G., In Bard, A. J., Rubenstein, I., Eds. *Electroanalytical Chemistry*; Marcel Dekker: NewYork, 1998; Vol. *20*, pp 227−294.

(6) Troyer, K. P.; Heien, M.; Venton, B. J.; Wightman, R. M. *Curr. Opin. Chem. Biol.* **2002**, *6*, 696−703.

(7) Wei, C.; Bard, A. J. *J. Electrochem. Soc.* **1995**, *142*, 2523−2527.

(8) Takii, Y.; Takoh, K.; Nishizawa, M.; Matsue, T. *Electrochim. Acta* **2003**, *48*, 3381−3385.

(9) Kurulugama, R. T.; Wipf, D. O.; Takacs, S. A.; Pongmayteegul, S.; Garris, P. A.; Baur, J. E. *Anal. Chem.* **2005**, *77*, 1111−1117.

(10) Hengstenber, A.; Blöchl, A.; Dietzel, I. D.; Schuhmann, W. *Angew. Chem., Int. Ed. Engl.* **2001**, *40*, 905−908.

(11) Kim, J.; Izadyar, A.; Nioradze, N.; Amemiya, S. *J. Am. Chem. Soc.* **2013**, *135*, 2321−2329.

(12) Bard, A. J.; Mirkin, M. V. *Scanning Electrochemical Microscopy*, 2nd ed.; CRC Press: Boca Raton, FL, 2012.

(13) Amemiya, S.; Guo, J.; Xiong, H.; Gross, D. A. *Anal. Bioanal. Chem.* **2006**, *386*, 458−471.

(14) Liu, X.; Ramsey, M. M.; Chen, X.; Koley, D.; Whiteley, M.; Bard, A. J. *Proc. Natl. Acad. Sci. U.S.A.* **2011**, *108* (7), 2668−2673.

(15) Koely, D.; Ramsey, M. M.; Bard, A. J.; Whiteley, M. *Proc. Natl. Acad. Sci. U.S.A.* **2011**, *108* (50), 19996−20001.

(16) Eibl, R.; Eibl, D.; Pörtner, R.; Catapano, G.; Czermer, P. *Cell and Tissue Reaction Engineering*; Springer-Verlag: Berlin, Heidelberg, 2009; pp 13−53.

(17) Connell, J. L.; Wessel, A.; Parsek, M. R.; Ellington, A. D.; Whiteley, M.; Shear, J. B. *mBio* **2010**, *1*, 1−8.

(18) Connell, J. L.; Ritschdorff, E. T.; Whiteley, M.; Shear, J. B. *Proc. Natl. Acad. Sci. U.S.A.* **2013**, *110* (46), 18380−18385.

(19) Wessel, A. K.; et al. *mBio* **2014**, *5* (2), No. e00992-14.

(20) Connell, J. L.; Kim, J.; Shear, J. B.; Bard, A. J.; Whiteley, M. *Proc. Natl. Acad. Sci. U.S.A.* **2014**, in press.

(21) Sambrook, J.; Maniatis, T.; Fritsch, E. F. *Molecular Cloning: A Laboratory Manual*, 2nd ed.; Cold Spring Harbor Laboratory: Cold Spring Harbor, N.Y., 1989.

(22) Palmer, K. L.; Mashburn, L. M.; Singh, P. K.; Whiteley, M. *J. Bacteriol.* **2005**, *187* (15), 5267−5277.

(23) Nielson, R.; Kaehr, B.; Shear, J. B. *Small* **2009**, *5* (1), 120−125.

(24) Kaehr, B.; Shear, J. B. *J. Am. Chem. Soc.* **2007**, *129* (7), 1904−1905.

(25) Nioradze, N.; Chen, R.; Kim, J.; Shen, M.; Santhosh, P.; Amemiya, S. *Anal. Chem.* **2013**, *85*, 6198−6202.

(26) Kaehr, B.; Shear, J. B. *Proc. Natl. Acad. Sci. U. S. A.* **2008**, *105*, 8850−8854.